Materials
Views
www.MaterialsViews.com
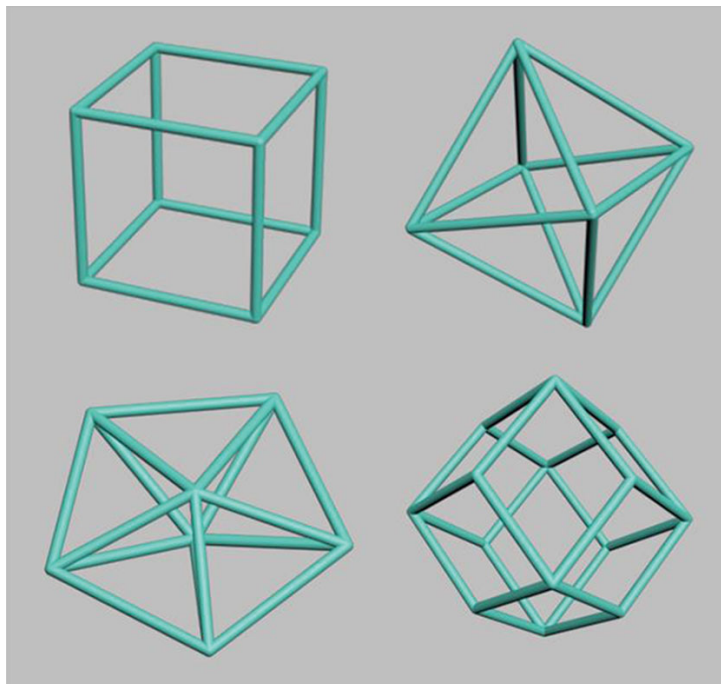
NANO MICRO
small

Nanoframes

Rational Design of Metal Nanoframes for Catalysis and Plasmonics

Zhicheng Fang, Youcheng Wang, Chenxuan Liu, Sheng Chen, Wei Sang, Chao Wang,* and Jie Zeng*

From the Contents

*R*ecently, metal nanoframes have received increased attention due to their unique spatial and physicochemical, e.g., catalytic and plasmonic properties. So far, a variety of synthetic procedures have been developed to fabricate metal nanoframes with different shapes, sizes and compositions. Typical synthesis of metal nanoframes involves two stages: 1) formation of solid nanocrystals and 2) hollowing out the interiors and side faces. In this review, solution-phase synthetic strategies are summarized, based on galvanic replacement reactions, oxidative etching, the Kirkendall effect, electrodeposition, and template-assisted growth, as well as one-pot synthesis. Their potential applications in catalysis and optical sensing are overviewed as well.

1. Introduction

Hollow metal nanostructures have gained extensive attention in recent decades, owing to their unique physicochemical properties that differ from their solid counterparts. They have also been acknowledged for a variety of applications, such as catalysis, optical sensing, and biomedicine.[1–9] So far, various morphologies of hollow metal nanocrystals have been explored, including nanoboxes, nanocages, nanoframes, and nanoshells.[10–17] Among those, nanoframes appear to have the most open structure when compared with other types of hollow nanostructures of similar sizes. In this work, "nanoframes" are referred as those nanocrystals composed of only ridges without side faces. In addition, nanocages with large cavity on side faces and nanodendrites consisting of multiple sheets can be called nanoframes as well.[18–20]

To date, thanks to the efforts of many research groups, various different shapes of nanoframes, including triangular, cubic, octahedral, and decahedral nanoframes have been prepared by either top-down or bottom-up methods.[21–24] For instance, Xia and co-workers demonstrated the synthesis of Au cubic nanoframes through a galvanic replacement reaction between $HAuCl_2$ and Ag.[25] In addition, a one-pot procedure to synthesize complex Au–Ag octahedral nanoframes has been proposed by Li and co-workers,[26] In general, synthesis of metal nanoframes mainly involves two stages. The first stage is the nucleation and growth of solid particles. The second stage is the hollowing out of the interiors and side faces, which could be achieved through galvanic replacement reactions or chemical etching.[22,27] The second stage, serving a crucial role in the formation of nanoframes, comes with certain challenges. Precise and selective removal of certain facets (or certain metals, for bimetallic nanoframes) while maintaining the frame structure is hard to achieve during galvanic reactions or etching processes. If the power of corrosion is too weak, hollowing could be incomplete, leading to partially open structures such as nanoboxes or nanocages.[28] In contrast, with powers of corrosion that are too strong, the nanoframes may be over-corroded and split into separate fragments.[29] Additionally, there are a few cases that take advantage of the Kirkendall effect to synthesize metal nanoframes.[30,31]

Metal nanoframes possess unique spatial structures that are promising for catalytic applications.[32–35] The 3D, network-like nature of nanoframes is structurally distinct from conventional high-surface-area heterogeneous catalysts. In the latter case, the high surface-area-to-volume ratio is gained by reducing the particle size, which inevitably deteriorates the stability of the catalysts. Nanoframes, however, provide a way to bypass this tradeoff. The removal of the non-functional atoms, buried in the interior, raises the specific surface area (per mass of metal) and improves the efficiency of utilizing the catalytic materials, particularly meaningful for scarce and precious metals. Compared with polyhedral nanoparticles of similar crystalline sizes (typically a few nanometers), the converged edges in nanoframes usually exhibit substantially enhanced thermal and chemical stability, partially due to the large overall size of the 3D object inherited from the solid particles formed in the first stage of synthesis. Unlike nanoboxes and nanoshells with enclosed exterior surface, the open 3D structures of nanoframes allow for molecular access to the interior surface atoms. This feature not only provides the advantage of high surface-to-volume ratio, but also brings about unconventional opportunities for tailoring the physical and chemical properties of heterogeneous catalysts and for achieving unprecedented catalytic performance.

In addition to excellent catalytic properties, their unique and tunable optical properties—and in particular their localized surface plasmon resonances (LSPR)—represent another attractive characteristic exhibited by metal nanoframes.[36–38] LSPR refers to the coherent oscillation of the free conduction band electrons in resonance with an incident electromagnetic field.[38–42] The LSPR peaks depend on various parameters, such as the shape, size, and dielectric environment of the nanoframe.[43–49] As observed by many groups, decreasing the ridge thickness and/or increasing the edge length will result in red-shifting of the resonance peak for Au cubic nanoframes.[25,38] The tunable LSPR property will render metal nanocrystals potentially useful in optical labels, near-field optical sensing, and as substrates for surface-enhanced Raman spectroscopy (SERS).[38,50–52]

In this review, typical synthetic strategies of metal nanoframes are first discussed. These strategies have been summarized and classified into three categories based on the relevant mechanisms applied during the nanoframe formation process: galvanic replacement reactions, oxidative etching, and the Kirkendall effect. Subsequently, the experimental operation strategies are classified into electrodeposition, template-assisted growth, and one-pot synthesis. In order to highlight the properties of metal nanoframes for remarkable applications in catalysis and optical sensing, a few examples are presented, before concluding with a summary and outlook.

2. Synthetic Strategies

2.1. Galvanic Replacement Reaction

It is well known that galvanic replacement reactions have been widely employed as simple and effective routes to synthesize metal nanocrystals with hollow interiors, including

Z. Fang, Y. Wang, C. Liu, S. Chen, W. Sang, Prof. J. Zeng
Hefei National Laboratory for Physical Sciences
at the Microscale and Key Laboratory of
Strongly-Coupled Quantum Matter Physics
of Chinese Academy of Sciences
Center of Advanced Nanocatalysis (CAN-USTC)
and Department of Chemical Physics
University of Science and Technology of China
Hefei, Anhui 230026, P. R. China
E-mail: zengj@ustc.edu.cn
Prof. C. Wang
Department of Chemical and Biomolecular Engineering
Johns Hopkins University
Baltimore, Maryland 21218, USA
E-mail: chaowang@jhu.edu

nanoboxes, nanocages and nanoframes.[53,54] During a galvanic replacement reaction, a template is oxidized and dissolved, while metal ions are reduced and the resultant atoms are deposited on the surface of the template. The driving force of the galvanic replacement reaction is the discrepancy in redox potential between the two metal species.[55,56] For instance, the reduction potential of AgCl/Ag (0.22 V vs standard hydrogen electrode (SHE)) is more positive than that of Zn^{2+}/Zn (−0.76 V vs SHE).[57] Thus, oxidation of Zn accompanied with reduction of AgCl can occur according to:

$$Zn(s) + 2AgCl(s) \rightarrow Zn^{2+} + 2Cl^- + 2Ag(s) \tag{1}$$
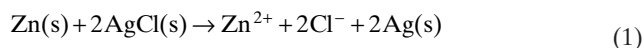
Ag is often selected to serve as a sacrificial template in many cases.[58–60] As a typical example, Xia and co-workers reported the formation of Au-based nanoframes via galvanic replacement reaction between Ag nanocubes and $HAuCl_2$.[25] The standard reduction potential of the $AuCl_2^-$/Au pair is 1.11 V (vs. SHE), which is higher than that of AgCl/Ag (0.22 V vs. SHE). Thus, the Ag nanocubes can be oxidized by $AuCl_2^-$. As shown in **Figure 1**A, Au was deposited on
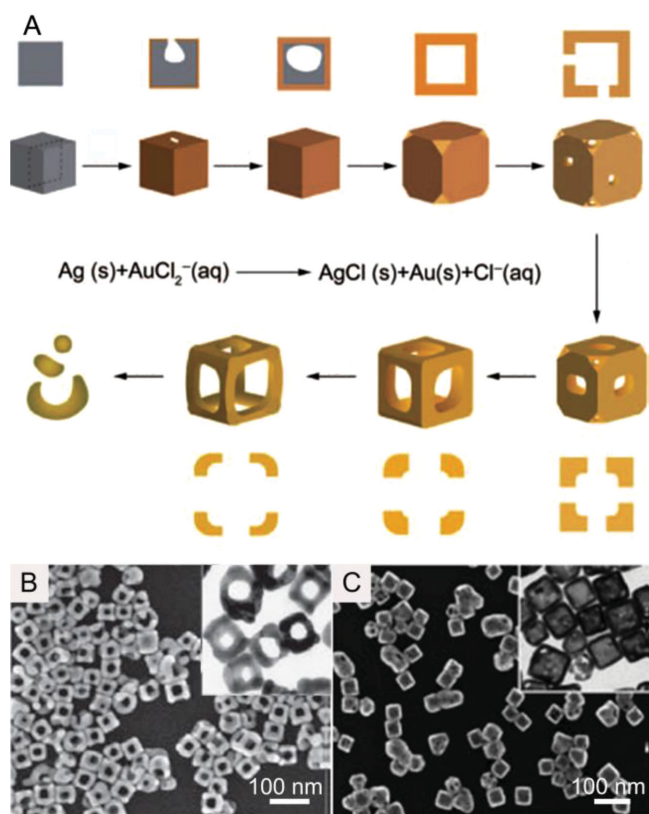

Figure 1. A) Scheme detailing the major differences in terms of morphological and structural changes during the galvanic replacement reaction involving Ag nanocubes and $AuCl_2^-$. The cross-sectional view corresponds to the plane along the dashed lines. Reproduced with permission.[25] Copyright 2008, Springer. B) SEM and TEM (insets) images showing samples obtained via galvanic replacement reaction involving Ag nanocubes with $AuCl_2^-$. Reproduced with permission.[25] Copyright 2008, Springer. C) SEM and TEM (insets) images showing samples obtained via galvanic replacement reaction involving Ag nanocubes with $AuCl_4^-$. Reproduced with permission.[61]

Zhicheng Fang received his BE degree in polymer materials from the Hefei University of Technology in 2014. He is currently a graduate student with Prof. Jie Zeng in the Hefei National Laboratory for Physical Sciences at the Microscale. His research interests include the design and synthesis of novel nanostructures and their use in catalysis.

Chao Wang received his BS in 2004 from the University of Science and Technology of China, and his PhD from Brown University in 2009. He worked as postdoc at Argonne National Laboratory before joining the faculty of the Department of Chemical and Biomolecular Engineering of Johns Hopkins University in 2012. His current research is focused on the design and synthesis of advanced nanomaterials for electrochemical energy conversion and storage applications, including CO_2 reduction, fuel cells and metal–air batteries.

Jie Zeng received his BS in Applied Chemistry at the University of Science and Technology of China (USTC) in 2002 and his PhD in Condensed Matter Physics (with Prof. Jianguo Hou) in 2007. He worked in Prof. Younan Xia's group as a postdoctoral fellow at Washington University in St. Louis from 2008 to 2011. Since 2012, he has held the position of Professor for Chemistry in the Hefei National Laboratory for Physical Sciences at the Microscale. His research interests include nanomaterials, heterogeneous catalysis, and surface chemistry.

the surface of a preformed Ag nanocube, while a pinhole appeared on one side face in the start stage due to the following galvanic replacement reaction:

$$Ag(s) + AuCl_2^-(aq) \rightarrow AgCl(s) + Au(s) + Cl^-(aq) \tag{2}$$
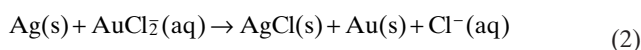
The pinhole was closed before long, leading to the formation of a seamless Au-Ag nanobox. The corners of the nanobox were truncated slightly. It should be pointed out that the generation of a truncated nanobox with a larger portion of {111} facets, instead of a nanobox with sharp corners, could be attributed to the order of the low-index crystallographic facets for a face-centered cubic (*fcc*) structure, namely, $\gamma_{\{110\}} > \gamma_{\{100\}} > \gamma_{\{111\}}$. With more $HAuCl_2$ added, a dealloying stage began, in which pores appeared at the corners and side faces simultaneously. Afterwards, the spontaneous migration of atoms to the more stable {111} facet
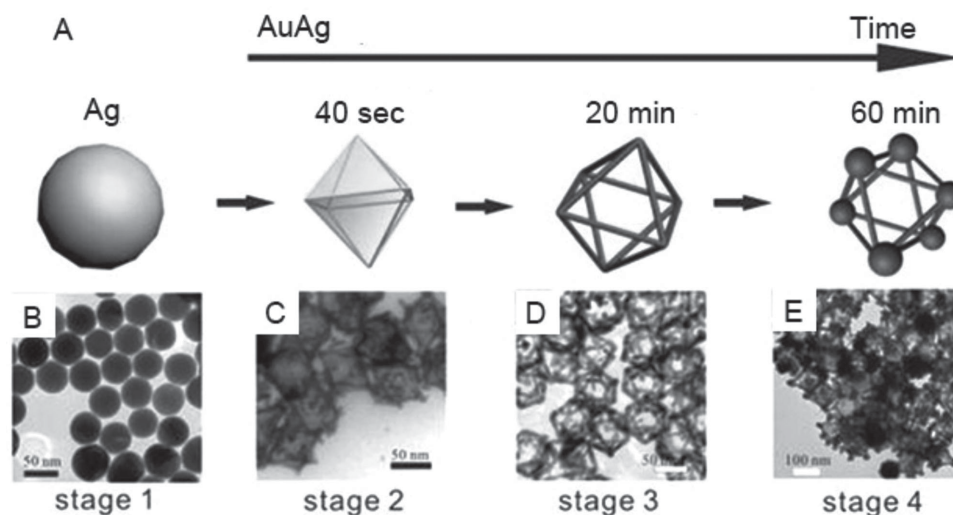
Figure 2. A) Schematic illustration of the deduced process of Au–Ag octahedral nanoframe formation. B) TEM image of Ag particles. C–E) TEM images of the products at different reaction times after HAuCl$_4$ is added: C) 40 s, D) 20 min, and E) 60 min. Reproduced with permission.[26] Copyright 2012, American Chemical Society.

resulted in the enlargement of pores at the side faces, accompanied by shrinkage of pores at the corners. Continuous migration resulted in the formation of a Au-based nanoframe (Figure 1B). When excess HAuCl$_2$ was added, the thickness of ridges further decreased due to dealloying of Ag atoms from the nanoframe. At a certain point, the ridges became so fragile that the nanoframe collapsed into fragments as a result. However, Xia and co-workers demonstrated that when an aqueous solution of HAuCl$_4$ instead of HAuCl$_2$ was added to react with the Ag nanocubes, Au-based nanocages with scattered and small pores on the surface (Figure 1C) could be obtained according to:

$$Ag(s) + AuCl_4^-(aq) \rightarrow AgCl(s) + Au(s) + 3Cl^-(aq) \qquad (3)$$
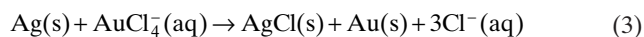
The standard reduction potential of the AuCl$_4^-$/Au pair (0.99 V vs. SHE) is higher than that of AgCl/Ag (0.22 V vs. SHE), so the Ag nanocubes can be oxidized in accordance with (3). The formation of Au-based nanoframes with a large pore on each side face when employing AuCl$_2^-$ contrasts to that of Au-based nanocages with scattered and small pores on the surface when employing AuCl$_4^-$, and this differencecan be attributed to the amount of Au(0) being deposited per each Ag(0) dissolved. It is known that AuCl$_2^-$ generates one Au(0) atoms per Ag(0) atom. As a result, the nanocages have much thicker edges, and they are robust enough to resist etching to form nanoframes during the dealloying process. On the other hand, AuCl$_4^-$ generates one Au(0) atom per every three Ag(0) atoms. Thus, the edges of the nanocages are extremely thin, and these nanocages would collapse into discrete particles easily instead of evolve into nanoframes during the dealloying process.[61]

In addition to cubic nanoframes, nanoframes with other shapes can also be obtained through galvanic replacement reactions. Li and co-workers reported the synthesis of Au-Ag octahedral nanoframes through the reduction of

AgNO$_3$ by copper(I) chloride and octadecylamine (ODA) at 115 °C, and subsequent addition of an aqueous solution of HAuCl$_4$.[26] As shown in **Figure 2**, a successive morphological transition from truncated Ag polyhedrons to octahedral hollow structures, and then to octahedral Au-Ag nanoframes, could be observed during the synthetic process. The galvanic replacement reaction between Ag and HAuCl$_4$, and selective deposition of resultant Au on the high-energy {110} facets, resulted in the change from truncated Ag polyhedrons to hollow Au-Ag octahedrons. The appearance of Au-Ag nanoframes was attributed to the fact that etching of Ag by AuCl$_4^-$ was easier for the stable {111} faces, while etching of the Ag in the sides of the octahedron was more difficult due to the covering of Ag with Au. When the reaction time was further increased, AuCl$_4^-$ and Ag$^+$ ions in the solution were co-reduced by ODA, and the resultant Au and Ag atoms selectively deposited on the corners of the octahedral nanoframes.

Nanoframes for other metals, not just Au, can be produced through galvanic replacement reactions as well. For instance, Tsuji et al. synthesized triangular Ag-Pd alloy nanoframes by galvanic replacement reaction between triangular Ag nanoplates and Na$_2$PdCl$_4$, with post-treatment using NaCl in an aqueous solution.[62] Recently, a similar example has been reported by Kawazumi and co-workers, who synthesized Pt-Ag alloy triangular nanoframes by galvanic replacement reactions followed by saturated NaCl treatment in an aqueous solution.[63]

In general, galvanic replacement reactions represent an effective and universal route to synthesize metal nanoframes. However, by far, most as-prepared nanoframes consist of alloy shells.[28] For instance, reviewing the Au-based nanoframes prepared through galvanic replacement reactions between Ag nanocubes and HAuCl$_2$, as presented in this section, the elemental composition was found to be was 89% Au and 11% Ag, as some Ag atoms could diffuse into the lattice of deposited Au.[25] Besides, it is difficult to precisely control

the ridge thickness of as-prepared nanoframes, as the galvanic replacement reaction involves dissolution of the template structures accompanied with simultaneous deposition on the surface of templates.[28]

2.2. Oxidative Etching

The formation of metal nanoframes through etching mainly involves selective dissolution of less stable elements and/or certain facets of the nanostructures with an appropriate etchant. Xia and co-workers synthesized cubic nanoframes consisting of pure Au by adding a certain amount of $Fe(NO_3)_3$ to selectively dissolve Ag from Au-Ag nanoboxes, made through galvanic replacement reaction between Ag nanocubes and $HAuCl_4$ (**Figure 3**).[28] An aqueous solution of $Fe(NO_3)_3$ can react with Ag according to

$$Ag(s) + Fe(NO_3)_3(aq) \rightarrow AgNO_3(aq) + Fe(NO_3)_2(aq) \quad (4)$$

Compared with the above protocol involving galvanic replacement reaction during the dealloying process, this new procedure allows more precise control over the ridge thickness and extent of hollowing of the resultant nanoframes. This could be attributed to the absence of concurrent deposition of Au in the dealloying process when using $Fe(NO_3)_3$ solution. It is known that Ag may not be completely etched away, due to the better etching resistance of Ag in the Ag-Au alloy than in pure Ag particles. This point has been proven by the observation that Ag atoms could not be completely extracted from Au/Ag alloy nanoboxes containing 30% Au, reacting with $Fe(NO_3)_3$. However, with the continuous addition of an aqueous $Fe(NO_3)_3$ solution, etching of nanoboxes with an atomic percentage of Au as low as 15%, could yield resultant products with an increased atomic ratio of 100:1 Au/Ag.[28] This observation is similar to the partial dissolution of Ag from a Au/Ag alloy with nitric acid reported by Espiell and co-workers, but the exact explanation remains elusive.[64] When NH_4OH was used as a wet etchant instead

of $Fe(NO_3)_3$, a mixture of nanocages and nanoframes was obtained. The difference in morphology results from different strengths of etchants. When NH_4OH is used, Au atoms can diffuse onto and passivate the Au/Ag alloy surface before complete removal of Ag atoms, as NH_4OH is a much weaker etchant than $Fe(NO_3)_3$.[65]

In addition to $Fe(NO_3)_3$ and NH_4OH mentioned above, O_2 is another common etchant. Previously, O_2 was used to synthesize hollow iron oxide and cobalt oxide nanoparticles through controlled oxidation of iron and cobalt nanoparticles, respectively.[66,67] Recently, Chen et al. demonstrated the synthesis of Pt_3Ni nanoframes based on the corrosion of $PtNi_3$ nanoparticles in the presence of O_2. First, they synthesized $PtNi_3$ polyhedrons with a uniform rhombic dodecahedral morphology.[35] Then, the $PtNi_3$ polyhedrons were dispersed in hexanes and kept under ambient conditions for 2 weeks, affording Pt_3Ni nanoframes. This evolution process could be accelerated by increasing the temperature to 120 °C. Finally, after dispersion of nanoframes onto carbon supports, and subsequent thermal treatment, Pt_3Ni nanoframes/C catalysts with Pt-skin surfaces were obtained. The schematic illustrations and corresponding transmission electron microscope (TEM) images of the samples at representative stages are presented in **Figure 4**. The evolution from $PtNi_3$ solid polyhedrons to Pt_3Ni nanoframes was ascribed to preferential oxidation of Ni on the facets by O_2, and dissolution of the formed nickel oxides in the presence of oleylamine ligands.[68] It is important to point out that the preferential etching in this process originated from the enrichment of Pt along the edges of the initial $PtNi_3$ particles, whereas the mechanism causing the uneven element distribution during the growth of solid $PtNi_3$ nanoparticles remains elusive.

Other oxidative etching routes include utilization of molten salt corrosion.[69] In general, the key to formation of nanoframes by oxidative etching is to control the speed and selectivity of etching. While the former is usually determined by the power of the etchant (e.g., chemical potential and concentration), reaction temperature, and similar factors, selective etching is usually more challenging and involves complicated mechanisms. Above all other parameters, the
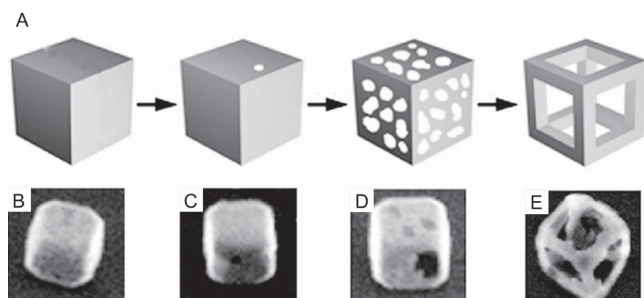

Figure 3. Schematic drawing and SEM images showing the formation of a Au cubic nanoframe. A) The schematic drawing for the formation of a Au cubic nanoframe. B) SEM image of an initial Ag nanocube; C) SEM image of a Au–Ag alloy nanobox obtained by reacting Ag nanocube with 4.0 mL of 0.2 mM $HAuCl_4$ aqueous solution; D,E) SEM images of the nanocage and nanoframe obtained by reacting the nanobox with 10 and 20 mL of 50 mM aqueous $Fe(NO_3)_3$ solution, respectively. Reproduced with permission.[28] Copyright 2007, American Chemical Society.
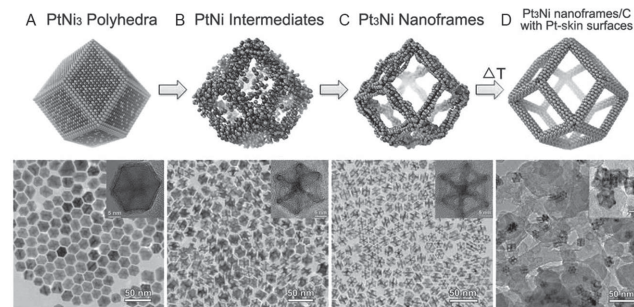

Figure 4. Schematic illustrations and corresponding TEM images of the products obtained at four representative stages during the evolution process from polyhedra to nanoframes. A) Initial solid $PtNi_3$ polyhedra. B) PtNi intermediates. C) Final hollow Pt_3Ni nanoframes. D) Annealed Pt_3Ni nanoframes with Pt(111)-skin-like surfaces dispersed on high-surface area carbon. Reproduced with permission.[35] Copyright 2014, AAAS.

power of the etchant seems to play a particularly important role: required to be neither too weak to accomplish complete corrosion/dealloying, nor too strong to diminish the selectivity and tear the nanoframes into fragments.

When employing either galvanic replacement reaction or oxidative etching, facet control is an inescapable problem. For a solid particle covered by only one type of facet, both galvanic replacement reactions and oxidative etching are expected to take place on this facet. When more than one type of facet is present on the surface of a solid particle, however, these two strategies can proceed with facet selectivity, which has significant connections with the surface energies of different facets. It has been established that the surface free energies of low-index facets of an fcc noble-metal crystal decrease in the order of $\gamma_{\{110\}} > \gamma_{\{100\}} > \gamma_{\{111\}}$. When a clean polyhedron with no capping agent on the surface is employed as the template for a galvanic replacement reaction or oxidative etching, the dissolution of atoms should begin from the {110} and {100} facets due to their higher surface free energy. However, a facet-specific capping agent is often intentionally introduced to cover the surface of a nanocrystal during its synthesis, which can alter the surface free energies of various facets, and even reverse their order.[53] Huang and co-workers have investigated chemical etching of Ag_2O nanocrystals by NH_3 solution and NaOH. They pointed out that the order of facet stability was found to be {111} > {110} > {100} due to the less effective adsorption of hydroxide ions on the {100} faces. As a result, the {100} facets are more susceptible to etching in comparison to other facets.[70,71] In addition to the capping agents, other factors such as reaction kinetics and twin defects can all affect the facet selectivity and thus deserve careful study.

2.3. Kirkendall Effect

The Kirkendall effect is a vacancy-mediated mechanism based on the observation of a net mass-flow of a faster diffusing species, balanced by the opposing flow of vacancies that condense into voids in solids.[72,73] It is a diffusion process involved in many synthetic processes of hollow and porous nanocrystals.[74–76] González et al. applied sequential galvanic replacement and Kirkendall effect reactions at room temperature to obtain polymetallic hollow nanocrystals with very different morphologies and compositions, such as double-walled Au-Ag nanoboxes, trimetallic Pd-Au-Ag nanoboxes and cylindrical hollow nanostructures. With small modifications to the synthetic protocol, they could also produce metal nanoframes, a kind of hollow nanocrystal.[30]

Very recently, Han et al. presented a unique structure transformation phenomenon for the fabrication of Cu_3Pt alloy nanoframes with polyhedral morphology. This strategy starts with the preparation of polyhedral Cu–Pt nanoparticles with a core-shell construction—formed by anisotropic growth of Pt on multiply twinned Cu seed particles—which are subsequently transformed into Cu_3Pt alloy nanoframes due to the Kirkendall effect between the Cu core and Pt shell. After the structural evolution, the as-prepared Cu_3Pt alloy nanoframes possess the rhombic dodecahedral morphology of their core–shell parents.[31]

2.4. Electrodeposition

Electrodeposition refers to the deposition of a substance on a substrate/electrode with the participation of electric current. In many works, electrodeposition has been employed to prepare solid particles with low porosity.[77] For instance, Pullini et al. reported the fabrication of Co/Cu-multilayer-nanowire arrays by pulsed electrodeposition into nanoporous polymer templates.[78] In this section, we focus on the preparation of metal nanoframes based on electrodeposition coupled with other methods, such as electroleaching and chemical etching.

Moghimi et al. demonstrated a unique route for synthesis of bimetallic FeNi nanoframes (nanocages with large cavity on each side face) through electrodeposition of FeNi particles from an electrolyte containing $NiCl_2$ and $FeCl_2$, followed by the process of electroleaching.[79] With increasing deposition time from 3 to 20 s, they observed that the morphological evolution of FeNi particles went from spherical particles to truncated cubes, to cubes with sharp corners, and finally to concave cubes (**Figure 5**A). Cl^- and Ni^{2+} ions in the solution increase the reduction rate of Fe^{2+} ions, leading to a kinetically controlled process of formation of concave nanocubes with exposed high-index facets. Later on, FeNi nanoframes were obtained by a controlled electroleaching process, hollowing out the interiors of the concave nanocubes. Since the point of highest surface energy is located at the center of the concave face, leaching and dissolution started at this site and continued to the edges until the center was completely hollowed out. Scanning electron microscope (SEM) images of the concave nanoframes obtained after one, two, and three cyclic voltammetry (CV) cycles are shown in Figure 5B–D, respectively.

Electrodeposition coupled with chemical etching can also be used to synthesize nanoframes. For instance, Okazaki et al. prepared Au nanoframes through selective electrodeposition of Au atoms on the edges and vertices of Ag cubes modified with
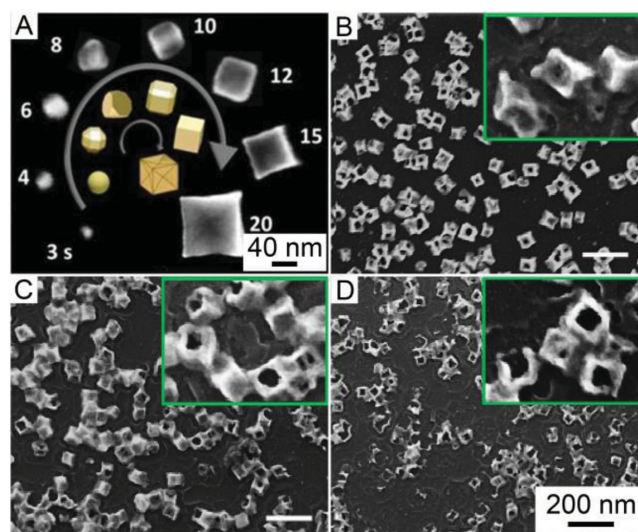

Figure 5. A) SEM images of typical FeNi nanocubes with increasing deposition time from 3 to 20 s. B–D) SEM images of FeNi nanocages obtained after one, two, and three CV cycles in a 10 mM PBS solution at pH 3 and a scan rate of 50 mV s^{-1}, respectively. Reproduced with permission.[79] Copyright 2013, American Chemical Society.
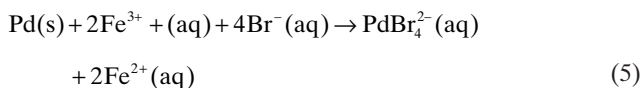
1-octanethiol, followed by chemical etching of the resulting particles with an aqueous solution containing H_2O_2 and H_2SO_4.[80]

2.5. Template-assisted Growth

Templating is a universal method of fabricating metal nanocrystals with various structures. For instance, Yu et al. synthesized Au@Pd concave nanocrystals enclosed by high-index Pd facets in the presence of Au trisoctahedrons as the template.[81] Xia and co-workers used a 3D porous lattice consisting of uniform iron particles as a template to generate gold multipods.[82] During the formation of nanoframes through template-assisted growth, the template serves as a scaffold and desirable materials can be added onto it (or generated in situ). Afterwards, an additional reaction stage is designed to remove the template completely. The as-prepared nanoframes can have shape and size corresponding to those of the parental template.

Xia and co-workers demonstrated a simple and effective route for synthesis of cubic Rh nanoframes through selective removal of Pd cores of the Pd–Rh nanocubes with Fe(III)/Br⁻ pairs as a wet etchant (**Figure 6**).[22] In this approach, Pd nanocubes served as a template. Site-specific nucleation and growth of Rh atoms at the corners and edges of the template resulted in the formation of Pd–Rh bimetallic nanocubes with a core–frame structure and concave side face. Selective adsorption of excess Br⁻ on the {100} side faces of preformed Pd cubic seeds, together with kinetically controlled growth achieved by adding Na_3RhCl_6, slowly led to preferential nucleation and selective growth at the corners and edges. Br⁻ also plays a crucial role in

Figure 6. A) TEM image of Rh cubic nanoframes obtained by selectively etching away the Pd cores from the Pd–Rh core–frame nanocubes; B,C) TEM images of Rh cubic nanoframes projected along <100> and <110> zone axes, respectively; and D) drawings showing 3D models of a Rh cubic nanoframe and its projections along <100>, <110>, and <111> zone axes. Reproduced with permission.[22]

the dealloying process. Complete etching of Pd nanocrystals is hard to achieve in the absence of Br⁻, because the difference in the standard reduction potentials between Fe(III)/Fe(II) and $PdCl_4^{2-}$/Pd pairs is too small (0.18 V vs SHE) to realize complete etching. When excess Br⁻ was added into the solution, the complete removal of Pd cubic cores can be achieved because the difference in the standard reduction potentials between Fe(III)/Fe(II) and $PdBr_4^{2-}$/Pd pair is much higher (0.28 V vs SHE), and the etching can occur according to

$$Pd(s) + 2Fe^{3+} + (aq) + 4Br^-(aq) \rightarrow PdBr_4^{2-}(aq)$$
$$+ 2Fe^{2+}(aq) \tag{5}$$

Recently, a similar route to synthesize ultrathin triangular gold nanoframes was demonstrated by Shahjamali et al.[21] In this method, Au atoms that were generated through reducing $HAuCl_4$ with hydroxylamine were selectively deposited on the edges of triangular Ag nanoplates. Etching of silver in the presence of a mixture solution containing H_2O_2 and NH_4OH was then performed.

Plate-like nanoframes can be considered as nanoplates having only edges, and no top or bottom faces. Jang et al. synthesized plate-like Pt nanoframes using Au nanoplates as a template.[83] They coated Ag atoms on the template and selectively etched Au and Ag from the core with dilute aqua regia. In this method, the galvanic replacement reaction between Ag atoms and Pt^{4+} primarily occurs at the edges, instead of the terraces, of nanoplates and Ag⁺ ions play the role of electron shuttle for Pt^{4+}.

Another typical example is the synthesis of ultrathin gold nanoframes through surfactant-free templating of pentagonal Ag nanocrystals, which was reported by McEachran et al.[24] In this approach, they performed selective deposition of Au atoms onto the decahedral silver templates, followed by dissolution of Ag from the Au-coated decahedra with H_2O_2. The morphological evolution and TEM images of samples at different stages were shown in **Figure 7**. It should be noted that different products were obtained when using gold-coated decahedrons containing different amounts of gold. Specifically, Au-based nanocages retaining some gold at both facets and edges were generated after reacting H_2O_2 with gold-coated decahedrons in which the amount of deposited gold was more than ca. 15%$_{Au/Ag}$ (where X%$_{Au/Ag}$ represents X molar percentage of gold relative to the silver present in the template). However, for the decahedrons in which the amount of deposited gold was less than ca. 15%$_{Au/Ag}$, the frame remained predominantly gold after treatment with H_2O_2. Dissolution and redeposition of Ag took place at a lower concentration of peroxide solution (approximately 0.05 M), forming Au–Ag alloy nanoframes. When using Ag templates with pentagonal twinning and {111} facets, such as icosahedrons and pentagonal faceted rods, corresponding nanoframes could also be synthesized using this procedure.

From the above examples, one can clearly see that a template method usually involves two major steps: growth of desirable metal on a preformed template, and removal of the template. A significant advantage of this method is that
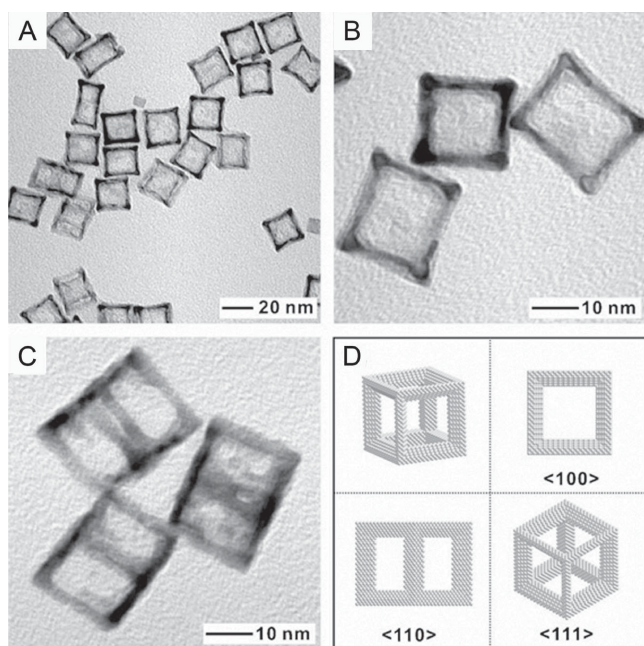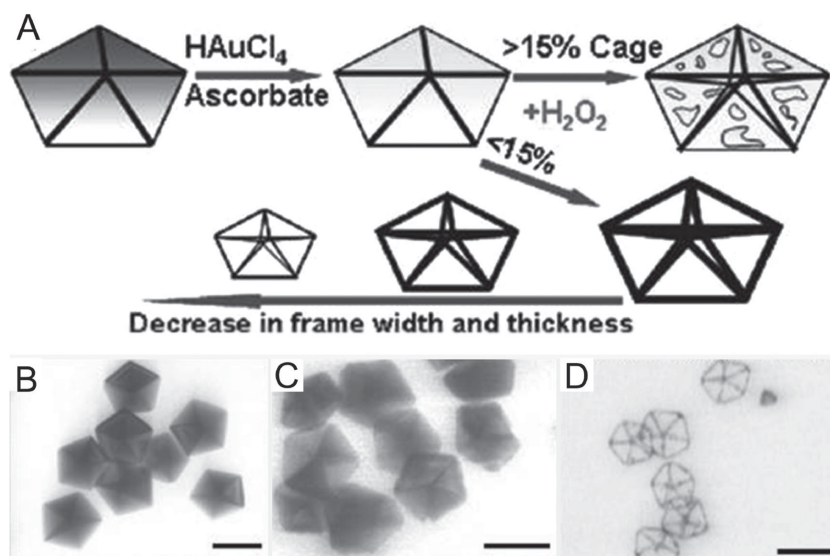
Figure 7. A) Illustration showing the formation of gold nanoframes and nanocages upon deposition of gold onto decahedral Ag-NPs, and subsequent silver dissolution with hydrogen peroxide. B) TEM image of silver decahedra prior to gold deposition. C) TEM image of silver decahedra after deposition of gold. D) TEM image of the frames after dissolution of silver with hydrogen peroxide. The amounts of gold deposited relative to silver in the template AgNPs were 5 mol%. All scale bars are 50 nm. Reproduced with permission.[24] Copyright 2011, American Chemical Society.

the morphology of the resulting nanoframes could be easily tuned by using templates with different shapes.

2.6. One-pot Synthesis

Although fabricating metal nanoframes with a one-pot method is simple and promising, there are far fewer reports regarding this method than templating. Among a variety of nanoframes synthesized using a one-pot strategy, Pt–Cu alloy nanoframes have been widely studied.[14,18,20] Recently, Zheng and co-workers reported the fabrication of unique excavated rhombic dodecahedral (ERD) PtCu$_3$ alloy nanocrystals (**Figure 8**) by co-reduction of the metal precursors Pt(acac)$_2$ and Cu(acac)$_2$ in the presence of

N,N-dimethylformamide (DMF), cetyltri-methylammonium chloride (CTAC) and n-butylamine.[20] The authors observed that ERD PtCu$_3$ nanocrystals were generated at the very early stage and then grew larger and larger as the reaction was prolonged. This evolution is totally different from the growth–etching process of the formation of metal nanoframes. The amine group in n-butylamine can selectively adsorb on {111} facets, leading to the different rates of growth along the <100> and <111> directions. Using a larger amount of n-butylamine, the area of exposed {110} facets on the resultant nanocrystals could be enlarged as well. Thus, a proper amount of n-butylamine is key to the formation of the ERD PtCu$_3$ alloy nanocrystals. It should be noted that the as-prepared ERD PtCu$_3$ nanocrystals are not conventional nanoframes with no side faces; they can be considered as frameworks constructed of 24 ultrathin nanosheets with high-energy {110} facets. Lou and co-workers demonstrated a one-pot solvothermal method to synthesize highly concave Pt nanoframes with an analogous shape.[84] Specifically, a solution containing H$_2$PtCl$_6$, oleylamine (OAm) and DMF underwent ultrasonication and heating at 160 °C for 12 h, and the resultant Pt nanoframes were enclosed by high-index {740} facets.

In addition to ERD alloy nanocrystals, cubic PtCu$_3$ nanoframes (nanocages with large cavities on each side face) could be generated using a one-pot method as well. Lou and co-workers reported the generation of PtCu$_3$ nanoframes through dissolution of H$_2$PtCl$_6$·6H$_2$O, Cu(acac)$_2$, and cetyltrimethylammonium bromide (CTAB) in OAm, with subsequent heating of the solution at 170 °C for 24h.[18] A typical high-magnification TEM image of the as-prepared PtCu$_3$ nanoframes is shown in **Figure 9**A. As the standard reduction potential of Cu(II)/Cu (0.34 V vs SHE) is more negative
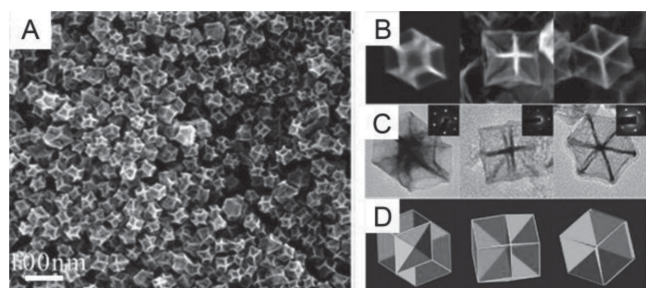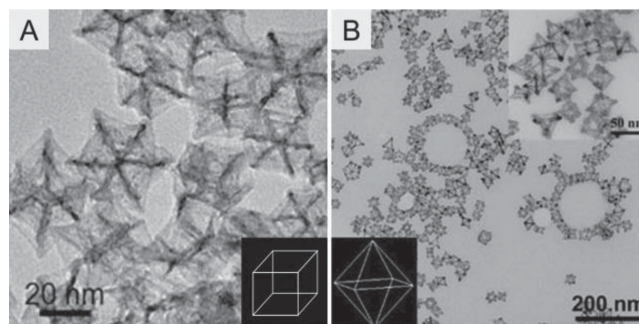

Figure 8. A) SEM image of the ERD PtCu$_3$ NCs on a large scale. B) SEM images, C) high-magnification TEM images showing an individual ERD PtCu$_3$ alloy NC with different orientations. Insets to (C) show the corresponding selected area electron diffraction patterns. D) Schematic models of an ERD PtCu$_3$ alloy NC viewed along the <110>, <100>, and <111> directions. Reproduced with permission.[20] Copyright 2014, American Chemical Society.

Figure 9. A) High-magnification TEM image of PtCu$_3$ cubic nanoframes and, inset, the corresponding model image. Adapted with permission.[18] Copyright 2012, American Chemical Society. B) TEM image of octahedral Pt–Cu nanoframes; top-right inset shows a high-magnification TEM image of octahedral Pt–Cu nanoframes, and the bottom-left inset shows the corresponding model image. Reproduced with permission.[14] Copyright 2013, Royal Society of Chemistry.

than that of Pt(II)/Pt (1.18 V vs SHE), Pt^{2+} should be reduced first. However, the authors proposed that Cu^{2+} ions are reduced first to form Cu nanocrystals, because CTAB could affect the reduction rates of Pt^{2+} and Cu^{2+} ions. Then, the galvanic replacement reaction between Cu nanocrystals and H_2PtCl_6 occurs spontaneously, leading to the formation of $PtCu_3$ hollow nanocages. Another similar example is the one-pot fabrication of single-crystalline octahedral Pt–Cu nanoframes (Figure 9B) demonstrated by Nosheen et al.[14] In this approach, $CuCl_2$, $H_2PtCl_6·6H_2O$, PVP glycine, NaI, and ethanolamine were respectively added to water, with the aqueous solution then heated at 200 °C for 2 h. Cu nanocrystals are formed ahead of Pt nanocrystals, as the presence of glycine above a certain threshold amount could influence the reduction rates of Pt^{2+} and Cu^{2+} ions. Afterwards, a galvanic replacement reaction between Cu nanocrystals and H_2PtCl_6 ions is responsible for the formation of octahedral Pt–Cu nanoframes.

3. Applications

3.1. Catalysis

Noble metals are widely used as catalysts in various chemical reactions.[85,86] A number of efforts have been made to enhance the performance of noble-metal catalysts, including tailoring their size, shape and composition.[87] Due to the unique spatial structure, nanoframes have the advantages of having large specific surface areas, high thermal and chemical stability, as well as unconventional surface atomic structures and 3D molecular accessibility.[35] Therefore, nanoframes made of noble metals have attracted great attention for catalytic applications.

The large specific surface areas of metal nanoframes usually give enhanced catalytic activity compared with their nanoparticulate counterparts. Li et al. applied single-crystalline octahedral Au–Ag nanoframes (discussed in Section 2.1) as catalysts for the synthesis of azobenzene from aniline.[26] A yield of 94% was obtained when the reaction was catalyzed by the Au–Ag nanoframes, while the yield was only 31% with the same amount of Au–Ag particles (with a diameter of ≈10 nm). Furthermore, the catalytic performance of metal nanoframes is strongly dependent on their surface structure.[88] Zheng et al. measured the catalytic properties of ERD nanocrystals with {110} facets preferrentially exposed, edge-concave octahedral $PtCu_3$ nanocrystals enclosed by {110} and {111} facets, octahedral $PtCu_3$ nanocrystals with {111}, and commercial Pt black. The metal nanocrystals with different facets often have distinct atomic bonding and surface activity. It was observed that the ERD $PtCu_3$ alloy nanocrystals with {110} surface showed the highest electrocatalytic activity, which was attributed to the smaller average coordination number of the atoms on this facet.[20] Although bimetallic nanoframes often exhibit excellent catalytic performance, detailed analysis and explanation regarding the catalytic properties of bimetallic nanoframes still deserve further work.

Electrochemical reactions, such as the oxygen reduction reaction (ORR) at the cathode of fuel cells and metal–air batteries, play a vital role in the development of renewable energy technologies. To raise the efficiency of electrical–chemical energy conversion and enable the large-scale implementation of these technologies, the catalytic activity and durability need to be substantially improved from current commercial electrocatalysts.[88–91] Very recently, Chen et al. reported a significantly improved performance of Pt_3Ni nanoframes (see Figure 4) compared with nanoparticulated PtNi/C and commercial Pt/C catalysts in the ORR.[35] The activity of different electrocatalysts follows the order: Pt/C < PtNi/C << Pt_3Ni nanoframes, as shown by the polarization curves given in **Figure 10**A. The Pt_3Ni nanoframes exhibited an improvement factor of >16 in specific activity (Figure 10C) and 22 in mass activity (Figure 10D) versus commercial Pt/C catalysts (both at 0.95 V vs. reversible hydrogen electrode (RHE)). The extraordinarily high specific activity of the Pt_3Ni nanoframes likely arises from the formation of the two-monolayer thick Pt-skin surface on the nanoframes, induced by controlled thermal treatment without destroying the 3D nanostructure, as well as the open structure of the Pt_3Ni nanoframes that allows access of the reactant molecules to both the internal and external surface atoms. Furthermore, the Pt_3Ni nanoframes were also shown to facilitate the incorporation of ionic liquids, e.g., [MTBD][NTf_2], into the electrocatalyst; further boosted catalytic activity was observed on the nanoframes/ionic liquid composite catalysts. Here the open 3D structure of the nanoframe is more efficient in fixing the ionic liquid than nanoparticulated catalysts, such as commercial Pt/C. The ionic liquid possesses high O_2 solubility and increases the O_2 concentration on the catalyst surface, raising the ORR activity.[32,34] Overall, the ionic liquid-encapsulated Pt_3Ni nanoframes exhibited an improvement factor of 22 in specific activity and 36 in mass activity versus Pt/C catalysts. In addition, the Pt_3Ni nanoframes were shown to be highly active for the hydrogen evolution reaction after surface modification with electrochemically deposited $Ni(OH)_2$ clusters, with enhancement of almost one order of magnitude relative to Pt/C (Figure 10B).

3.2. Optical Properties and Applications

Metal nanoframes have unique optical properties, due to their localized surface plasmon resonances (LSPR), involving the coherent oscillation of the free conduction band electrons in resonance with an incident electromagnetic field.[38–42] In comparison to other morphologies, metal nanoframes have distinct LSPR properties. Cheng and co-workers have investigated the plasmon modes of Ag nanoboxes, nanocages, and nanoframes. The results show that the plasmon modes (dipole and quadrupole) of a single Ag nanocage are red-shifted relative to the nanobox as the surface porosity of the nanocage increases. In particular, the wavelengths at the peaks of these modes almost linearly depend on the surface porosity: the larger the surface porosity, the more the red-shifted these modes. For a Ag nanoframe whose hole length on the side faces is larger than half of the edge length, the dipole mode is within the near-infrared regime.[92] Xia and co-workers observed UV–vis spectra of the intermediate
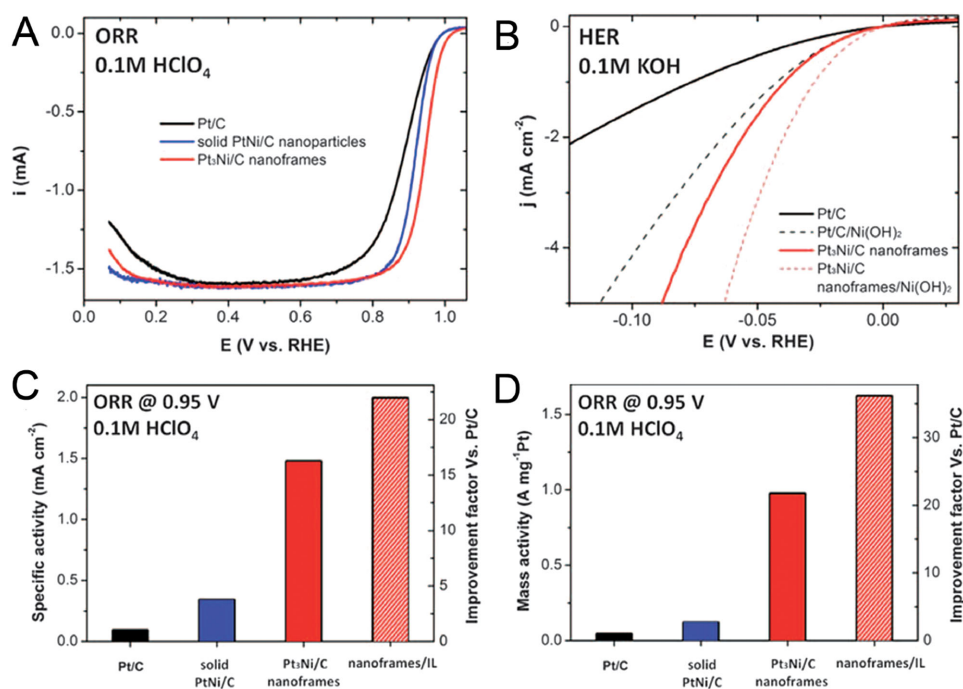
Figure 10. Electrochemical properties of Pt$_3$Ni nanoframes. A) Cyclic voltammograms of Pt/C and Pt$_3$Ni/C nanoframes signify the difference in surface coverage by H$_{upd}$ and OH$_{ad}$. Electrochemically active surface area (ECSA) of the nanoframes is determined by integrated charge of adsorbed CO electro-oxidation curve. B) Hydrogen evolution reaction (HER) activities for Pt/C, Pt/Ni(OH)$_2$/C, Pt$_3$Ni nanoframes/C, and Pt$_3$Ni frames/Ni(OH)$_2$/C in alkaline electrolyte. C,D) Specific (C) and mass (D) activities measured at 0.95 V, and improvement factors versus Pt/C catalysts. Because of the high intrinsic activity of the Pt$_3$Ni nanoframes, the ORR activity values are given at 0.95 V in order to avoid the extensive error margin at 0.9 V introduced by the close proximity of current values to the diffusion-limited current. Note: IL is shorthand for ionic liquid. Reproduced with permission.[35] Copyright 2014, AAAS.

products prepared through the galvanic replacement reaction between Ag nanocubes and different amounts of HAuCl$_2$ (discussed in Section 2.1).[25] During the synthetic process, a significant LSPR red-shifting of the intermediates was observed with increasing amounts of HAuCl$_2$ as shown in **Figure 11**A. In addition, they summarized the scattering spectra of the as-prepared gold nanoframes in Figure 11B with the SEM images of the corresponding nanoframes in the inset. As the ratio *R* between the outer edge length and the ridge thickness increased, the peak position was red-shifted. This is because an increase in edge length or a decrease in ridge thickness increases the charge separation, leading to the reduction of the restoring force for electron oscillation. In addition to the size, it is established that the composition has significant effects on the LSPR properties as well. For instance, Polavarapu et al. reported that the morphological and compositional changes involved in the galvanic replacement reaction between Ag nanocubes and HAuCl$_4$ in organic media led to changes in the LSPR of the resultant Au–Ag particles. With the continuous addition of HAuCl$_4$ into the reaction mixture, the final Ag/Au molar ratios in the products increases,and significant LSPR red-shifts can be observed. However, excess addition of HAuCl$_4$ leads to a blue shift due to fragmentation of the hollow nanostructures.[36]

Due to the unique and tunable LSPR property, nanoframes have potential applications in optical sensing.

Mahmoud et al. studied the sensing efficiency of gold nanoframes prepared using Ag nanocube templates to react with HAuCl$_4$.[38] The efficiency of a near-infrared sensor is measured by the sensitivity factor *S*, which is defined as the shift in the wavelength of the surface plasmon resonance (SPR) peak position (in nanometers) per unit change in the refractive index (RIU) of the surrounding medium. The shift of the SPR peak position of gold nanoframes can reflect the change in the dielectric constant of the surrounding environment when the shape, size, and interparticle separation are fixed. Figure 11C shows the SPR spectra of gold nanoframes with a wall length *L* of 42 nm and a wall thickness *T* of 9 nm assembled as monolayers on the surface of quartz substrates measured in different solvents. It can be clearly seen that gold nanoframes have different peaks in different surroundings. Specifically, with increasing refractive index of the solvent, a red shift of the SPR for these nanoframes was observed. The relationship between the refractive index of the solvent and the SPR peak maximum of Au nanoframes was found to be linear. With increasing the aspect ratio *L/T* of the Au nanoframes, the sensitivity factors (the slopes of the straight lines between λ_{max} and the refractive index) also increased. The strong surface plasmonic fields of hollow nanoframes, resulting from the coupling between the surface plasmonic fields on the exterior and interior walls, may be related to the high sensitivity factors of gold nanoframes.
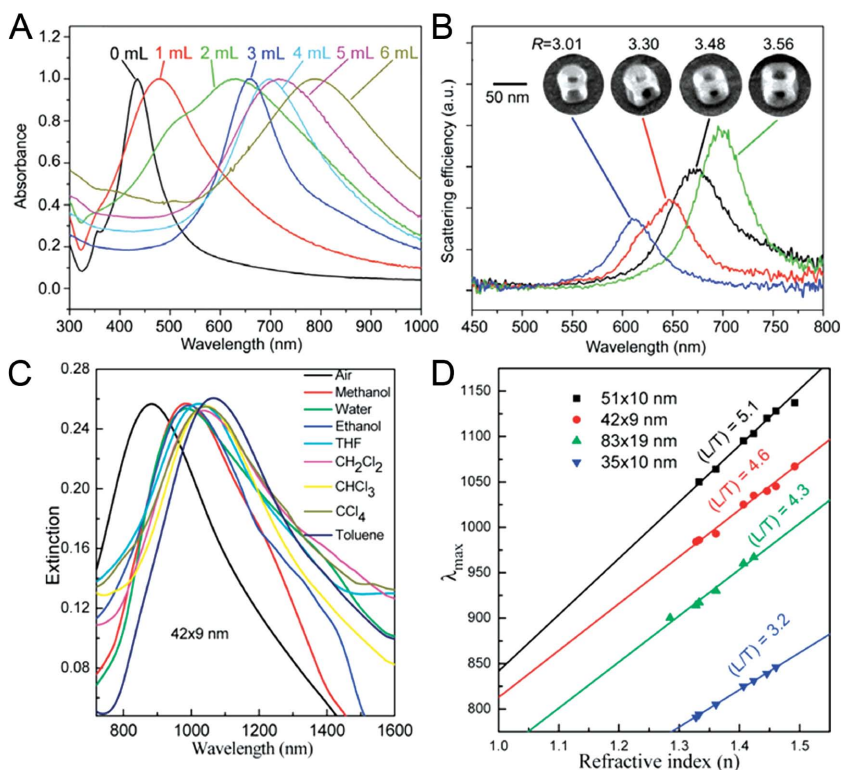
Figure 11. A) UV–vis spectra taken from aqueous suspensions of the structures synthesized by titrating Ag nanocubes with 1 mL to 6 mL of 0.1 mM/L $AuCl_2^-$. Reproduced with permission.[25] Copyright 2008, Springer. B) Scattering spectra of individual Au nanoframes and corresponding SEM. Reproduced with permission.[25] Copyright 2008, Springer. C) SPR of 42 nm wall-length and 9 nm wall-thickness Au nanoframe monolayers assembled on the surface of quartz substrates and measured in different solvents. Reproduced with permission.[38] Copyright 2010, American Chemical Society. D) Relationship between the refractive index and the SPR peak maximum of Au nanoframes with different aspect ratios. This figure also shows that the values of the sensitivity factors (determined from the slope of each line for each aspect ratio) are 620 ± 15, 516 ± 24, 508 ± 33, and 409 ± 6 for nanoframes of aspect ratios 5.1, 4.6, 4.3, and 3.2, respectively. Reproduced with permission.[38] Copyright 2010, American Chemical Society.

4. Summary and Outlook

During the past decade, metal nanoframes have received increasing attention due to their unique spatial structures and physicochemical properties. Substantial progress has been made in both controlled synthesis and demonstration of functional applications of metal nanoframes. In this review, we summarized five categories of typical synthetic strategies for nanoframes: 1) galvanic replacement reaction, 2) oxidative etching, 3) Kirkendall effect, 4) electrodeposition, 5) template-assisted growth, and 6) one-pot synthesis. It has been shown that nanoframes with diverse morphologies for different metals, including triangular Au–Pd, cubic Rh, octahedral Au–Ag, and rhombic dodecahedral Pt_3Ni nanoframes have been obtained through the above strategies. Applications of these open, three-dimensional nanostructures have been discussed in terms of catalysis and optical sensing. It has been illustrated that metal nanoframes usually possess superior catalytic properties in chemical reactions and a high sensitivity factor in optical sensing.

Despite the progress that has been made, challenges are still present in the controlled synthesis of metal nanoframes for tuning the degree of hollowing, thickness of ridges, and elemental composition. In particular, controlling the ridge thickness of metal nanoframes is of great significance since this parameter is unique and critical to catalytic and plasmonic properties. One feasible route is the tuning of the thickness of deposited metals on a template by adjusting the relative amount of metal precursors and templates. Another practical route is adjustment of the certain parameters, including temperature, etching time, type and amount of additives, and so on, during the etching process to control the extent to which solid particles are hollowed out. Fundamental understanding of the growth mechanisms of nanoframes is yet to be developed, which has limited the selectivity in carving the three-dimensional morphology. To overcome these challenges, integration of different synthetic strategies, e.g., template growth and oxidative etching, as discussed in section 2.5, or development of new methods, is needed. Theoretical studies for simulation of the nanostructure evolution during the synthesis, which to a large extent are still missing, would also be important for gaining insight into the process of nanoframes formation, and providing guidance for the future studies. Meanwhile, production of nanoframes so far has mostly been limited to the milligram scale. The present yields are obviously insufficient for meeting industrial demands for catalytic materials. Therefore, another focus of future work should be on exploiting more robust synthesis that could enable the scaled-up production of nanoframes.

Although they have been demonstrated to be advantageous in catalysis and optical sensing, the structure–property relationships of metal nanoframes in these applications are yet to be established and understood. Though it is clear that the factors that have significant effects on the catalysis are complicated and entangled with each other, classification of the catalytic functions has not, in most cases, discovered the extent to which this is the case. More related work towards this question is expected in the future. Besides the demonstrated applications, the open three-dimensional nanostructures could be utilized to load drug and biological molecules for targeted delivery. The facilitated formation of composite nanostructures with other materials, as demonstrated in the case of Pt_3Ni nanoframes/ionic liquid, could also be exploited for other catalytic reactions. With the continuation and growth of research into metal nanoframes, futher functionalites and more promising performances in existing functionalities may be expected for various applications.

Acknowledgments

[1] S.-W. Kim, M. Kim, W. Y. Lee, T. Hyeon, *J. Am. Chem. Soc.* **2002**, *124*, 7642.

[2] H. M. Chen, R. S. Liu, M. Y. Lo, S. C. Chang, L. D. Tsai, Y. M. Peng, J. F. Lee, *J. Phys. Chem. C* **2008**, *112*, 7522.

[3] H. Zhang, M. Jin, H. Liu, J. Wang, M. J. Kim, D. Yang, Z. Xie, J. Liu, Y. Xia, *ACS Nano* **2011**, *5*, 8212.

[4] S. Lal, S. Link, N. J. Halas, *Nat. Photonics* **2007**, *1*, 641.

[5] J. Zeng, J. Huang, W. Lu, X. Wang, B. Wang, S. Zhang, J. Hou, *Adv. Mater.* **2007**, *19*, 2172.

[6] W. Li, X. Cai, C. Kim, G. Sun, Y. Zhang, R. Deng, M. Yang, J. Chen, S. Achilefu, L. V. Wang, Y. Xia, *Nanoscale* **2011**, *3*, 1724.

[7] K. Niikura, N. Iyo, Y. Matsuo, H. Mitomo, K. Ijiro, *ACS Appl. Mater. Interfaces* **2013**, *5*, 3900.

[8] S. Shukla, A. Priscilla, M. Banerjee, R. R. Bhonde, J. Ghatak, P. V. Satyam, M. Sastry, *Chem. Mater.* **2005**, *17*, 5000.

[9] C. Zhou, T. H. Tsai, D. C. Adler, H. C. Lee, D. W. Cohen, A. Mondelblatt, Y. Wang, J. L. Connolly, J. G. Fujimoto, *Opt. Lett.* **2010**, *35*, 700.

[10] B. T. Sneed, C. N. Brodsky, C. H. Kuo, L. K. Lamontagne, Y. Jiang, Y. Wang, F. Tao, W. Huang, C. K. Tsung, *J. Am. Chem. Soc.* **2013**, *135*, 14691.

[11] A. Popa, A. C. S. Samia, *Chem. Commun.* **2014**, *50*, 7295.

[12] P. Shi, M. Li, J. Ren, X. Qu, *Adv. Funct. Mater.* **2013**, *23*, 5338.

[13] M. A. Mahmoud, M. A. El-Sayed, *Langmuir* **2012**, *28*, 4051.

[14] F. Nosheen, Z. Zhang, J. Zhuang, X. Wang, *Nanoscale* **2013**, *5*, 3660.

[15] H.-J. Jang, S. Hong, S. Park, *J. Mater. Chem.* **2012**, *22*, 19792.

[16] J. Zhang, Y. Fu, F. Mahdavi, *J. Phys. Chem. C* **2012**, *116*, 24224.

[17] K. G. S. Ranmohotti, X. Gao, I. U. Arachchige, *Chem. Mater.* **2013**, *25*, 3528.

[18] B. Y. Xia, H. B. Wu, X. Wang, X. W. Lou, *J. Am. Chem. Soc.* **2012**, *134*, 13934.

[19] N. Moghimi, M. Abdellah, J. P. Thomas, M. Mohapatra, K. T. Leung, *J. Am. Chem. Soc.* **2013**, *135*, 10958.

[20] Y. Jia, Y. Jiang, J. Zhang, L. Zhang, Q. Chen, Z. Xie, L. Zheng, *J. Am. Chem. Soc.* **2014**, *136*, 3748.

[21] M. M. Shahjamali, M. Bosman, S. Cao, X. Huang, X. Cao, H. Zhang, S. S. Pramana, C. Xue, *Small* **2013**, *9*, 2880.

[22] S. F. Xie, N. Lu, Z. X. Xie, J. G. Wang, M. J. Kim, Y. N. Xia, *Angew. Chem. Int. Ed.* **2012**, *51*, 10266.

[23] F. Nosheen, Z.-C. Zhang, J. Zhuang, X. Wang, *Nanoscale* **2013**, *5*, 3660.

[24] M. McEachran, D. Keogh, B. Pietrobon, N. Cathcart, I. Gourevich, N. Coombs, V. Kitaev, *J. Am. Chem. Soc.* **2011**, *133*, 8066.

[25] L. Au, Y. C. Chen, F. Zhou, P. H. C. Camargo, B. Lim, Z. Y. Li, D. S. Ginger, Y. Xia, *Nano Res.* **2008**, *1*, 441.

[26] X. Hong, D. Wang, S. Cai, H. Rong, Y. Li, *J. Am. Chem. Soc.* **2012**, *134*, 18165.

[27] D. Wan, X. Xia, Y. Wang, Y. Xia, *Small* **2013**, *9*, 3111.

[28] X. Lu, L. Au, J. McLellan, Z.-Y. Li, M. Marquez, Y. Xia, *Nano Lett.* **2007**, *7*, 1764.

[29] S. E. Skrabalak, J. Chen, Y. Sun, X. Lu, L. Au, C. M. Cobley, Y. Xia, *Acc. Chem. Res.* **2008**, *41*, 1587.

[30] E. González, J. Arbiol, V. F. Puntes, *Science* **2011**, *334*, 1377.

[31] L. Han, H. Liu, P. Cui, Z. Peng, S. Zhang, J. Yang, *Sci. Rep.* **2014**, *4*, 6414.

[32] J. Snyder, T. Fujita, M. W. Chen, J. Erlebacher, *Nat. Mater.* **2010**, *9*, 904.

[33] J. Snyder, I. McCue, K. Livi, J. Erlebacher, *J. Am. Chem. Soc.* **2012**, *134*, 8633.

[34] J. Snyder, K. Livi, J. Erlebacher, *Adv. Funct. Mater.* **2013**, *23*, 5494.

[35] C. Chen, Y. Kang, Z. Huo, Z. Zhu, W. Huang, H. L. Xin, J. D. Snyder, D. Li, J. A. Herron, M. Mavrikakis, M. Chi, K. L. More, Y. Li, N. M. Markovic, G. A. Somorjai, P. Yang, V. R. Stamenkovic, *Science* **2014**, *343*, 1339.

[36] L. Polavarapu, L. M. Liz-Marzán, *Nanoscale* **2013**, *5*, 4355.

[37] M. A. Mahmoud, M. A. El-Sayed, *Nano Lett.* **2009**, *9*, 3025.

[38] M. A. Mahmoud, M. A. El-Sayed, *J. Am. Chem. Soc.* **2010**, *132*, 12704.

[39] S. Zou, G. C. Schatz, *Chem. Phys. Lett.* **2005**, *403*, 62.

[40] S. J. Oldenburg, R. D. Averitt, S. L. Westcott, N. J. Halas, *Chem. Phys. Lett.* **1998**, *288*, 243.

[41] H. Wang, D. W. Brandl, P. Nordlander, N. J. Halas, *Acc. Chem. Res.* **2007**, *40*, 53.

[42] P. K. Jain, X. Huang, I. H. El-Sayed, M. A. El-Sayed, *Acc. Chem. Res.* **2008**, *41*, 1578.

[43] J. Zhao, A. O. Pinchuk, J. M. McMahon, S. Li, L. K. Ausman, A. L. Atkinson, G. C. Schatz, *Acc. Chem. Res.* **2008**, *41*, 1710.

[44] L. J. Sherry, R. Jin, C. A. Mirkin, G. C. Schatz, R. P. Van Duyne, *Nano Lett.* **2006**, *6*, 2060.

[45] I. H. El-Sayed, X. Huang, M. A. El-Sayed, *Nano Lett.* **2005**, *5*, 829.

[46] A. J. Haes, S. Zou, G. C. Schatz, R. P. Van Duyne, *J. Phys. Chem. B* **2004**, *108*, 109.

[47] J.-J. Storhoff, A.-A. Lazarides, R.-C. Mucic, C.-A. Mirkin, R.-L. Letsinger, G.-C. Schatz, *J. Am. Chem. Soc.* **2000**, *122*, 4640.

[48] A. J. Haes, S. Zou, G. C. Schatz, R. P. Van Duyne, *J. Phys. Chem. B* **2004**, *108*, 6961.

[49] J. Zhao, A. J. Haes, X. Zhang, S. Zou, E. M. Hicks, G. C. Schatz, R. P. Van Duyne, in *MRS Symp. Proc., Vol. 900* (Eds: C-J. Zhong, N. A. Kotov, W. Daniell, F. P. Zamborini), Cambridge University Press, Cambridge, UK **2006**.

[50] A. J. Haes, C. L. Haynes, A. D. McFarland, G. C. Schatz, R. R. Van Duyne, S. L. Zou, *MRS Bull.* **2005**, *30*, 368.

[51] A. D. McFarland, R. P. Van Duyne, *Nano Lett.* **2003**, *3*, 7426.

[52] C. L. Haynes, R. P. Van Duyne, *J. Phys. Chem. B* **2003**, *107*, 7426.

[53] X. Xia, Y. Wang, A. Ruditskiy A, Y. Xia, *Adv. Mater.* **2013**, *25*, 6313.

[54] X. Teng, Q. Wang, P. Liu, W. Han, A. I. Frenkel, W. Wen, N. Marinkovic, J. C. Hanson, J. A. Rodriguez, *J. Am. Chem. Soc.* **2008**, *130*, 1093.

[55] Y. Sun, Y. Xia, *J. Am. Chem. Soc.* **2004**, *126*, 3892.

[56] Y. Sun, B. Mayers, Y. Xia, *Adv. Mater.* **2003**, *15*, 641.

[57] G. Inzelt, *Encyclopedia of Electrochemistry*, *Vol. 7* (Eds: A. J. Bard, M. Stratmann, F. Scholz, C. J. Pickett), Wiley-VCH, Weinheim, Germany **2006**, p. 43.

[58] H. M. Chen, R. S. Liu, M. Y. Lo, S. C. Chang, L. D. Tsai, Y. M. Peng, J. F. Lee, *J. Phys. Chem. C* **2008**, *112*, 7522.

[59] N. R. Sieb, N. C. Wu, E. Majidi, R. Kukreja, N. R. Branda, B. D. Gates, *ACS Nano* **2009**, *3*, 1365.

[60] M. H. Kim, X. Lu, B. Wiley, E. P. Lee, Y. Xia, *J. Phys. Chem. C* **2008**, *112*, 7872.

[61] L. Au, X. Lu, Y. Xia, *Adv. Mater.* **2008**, *20*, 2517.

[62] M. Tsuji, T. Kidera, A. Yajima, M. Hamasaki, M. Hattori, T. Tsuji, H. Kawazumi, *CrystEngComm* **2014**, *16*, 2684.

[63] M. Tsuji, M. Hamasaki, A. Yajima, M. Hattori, T. Tsuji, H. Kawazumi, *Mater. Lett.* **2014**, *121*, 113.

[64] L. L. Martinez, M. Segarra, M. Fernandez, F. Espiell, *Metall. Trans. B* **1993**, *24*, 827.

[65] Y. Xia, E. Kim, G. M. Whitesides, *J. Electrochem. Soc.* **1996**, *143*, 1070.

[66] Y. D. Yin, R. M. Rioux, C. K. Erdonmez, S. Hughes, G. A. Somorjai, A. P. Alivisatos, *Science* **2004**, *304*, 711.

[67] J. Yang, C.-H. Lee, H.-J. Ko, J.-S. Suh, H.-G. Yoon, K. Lee, Y.-M. Huh, S. Haam, *Angew. Chem. Int. Ed.* **2007**, *46*, 8836.

[68] D. Wang, Y. Li, *Inorg. Chem.* **2011**, *50*, 5196.

[69] D. Kim, J. Park, K. An, N. K. Yang, J. G. Park, T. Hyeon, *J. Am. Chem. Soc.* **2007**, *129*, 5812.

[70] L.-M. Lyu, M. H. Huang, *J. Phys. Chem. C* **2011**, *115*, 17768.

[71] M. H. Huang, S. Rej, S.-C. Hsu, *Chem. Commun.* **2014**, *50*, 1634.

[72] A. Smigelakas, E. Kirkendall, *Trans. Aime* **1947**, *171*, 130.

[73] J. X. Wang, C. Ma, Y. Choi, D. Su, Y. Zhu, P. Liu, R. Si, M. B. Vukmirovic, Y. Zhang, R. R. Adzic, *J. Am. Chem. Soc.* **2011**, *133*, 13551.

[74] H. J. Fan, U. Gosele, M. Zacharias, *Small* **2007**, *3*, 1660.

[75] H. M. Chen, R. S. Liu, *J. Phys. Chem. C* **2011**, *115*, 3513.

[76] Y. S. Hu, Y. G. Guo, W. Sigle, S. Hore, P. Balaya, J. Maier, *Nat. Mater.* **2006**, *5*, 713.

[77] U. Erb, *Nanostruct. Mater.* **1995**, *6*, 533.

[78] D. Pullini, D. Busquets-Mataix, *ACS Appl. Mater. Inter.* **2011**, *3*, 759.

[79] N. Moghimi, M. Abdellah, J. P. Thomas, M. Mohapatra, K. T. Leung, *J. Am. Chem. Soc.* **2013**, *135*, 10958.

[80] K.-i. Okazaki, J.-i. Yasui, T. Torimoto, *Chem. Commun.* **2009**, 2917.

[81] Y. Yu, Q. Zhang, B. Liu, J. Y. Lee, *J. Am. Chem. Soc.* **2013**, *132*, 18258.

[82] Z. Li, W. Li, P. H. C. Camargo, Y. Xia, *Angew. Chem.* **2008**, *120*, 9799.

[83] H.-J. Jang, S. Hong, S. Park, *J. Mater. Chem.* **2012**, *22*, 19792.

[84] B. Y. Xia, H. B. Wu, X. Wang, X. W. Lou, *Angew. Chem. Int. Ed.* **2013**, *52*, 12337.

[85] S. Guo, E. Wang, *Nano Today* **2011**, *6*, 240.

[86] A. Mohanty, N. Garg, R. C. Jin, *Angew. Chem. Int. Ed.* **2010**, *49*, 4962.

[87] S. Xie, S.-I. Choi, X. Xia, Y. Xia, *Curr. Opin. Chem. Eng.* **2013**, *2*, 142.

[88] N. M. Marković, P. N. Ross, *Surf. Sci. Rep.* **2002**, *45*, 117.

[89] J. K. Nørskov, J. Rossmeisl, A. Logadottir, L. Lindqvist, J. R. Kitchin, T. Bligaard, H. Jonsson, *J. Phys. Chem. B* **2004**, *108*, 17886.

[90] H. A. Gasteiger, S. S. Kocha, B. Sompalli, F. T. Wagner, *Appl. Catal. B* **2005**, *56*, 9.

[91] V. R. Stamenkovic, B. Fowler, B. S. Mun, G. Wang, P. N. Ross, C. A. Lucas, N. M. Markovic, *Science* **2007**, *315*, 493.

[92] C. Ma, R. Zhang, J.-W. Liaw, J. C. Cheng, *Appl. Phys. A* **2014**, *115*, 31.